GLOBAL CLOUD PROPERTY MODELS FOR REAL TIME TRIAGE ONBOARD VISIBLE-SHORTWAVE INFRARED SPECTROMETERS

A FINAL REPORT SUBMITTED TO THE DEPARTMENT OF EARTH SCIENCES, UNIVERSITY OF HAWAI’I AT MĀNOA, IN PARTIAL FULFILLMENT OF THE REQUIREMENTS FOR THE DEGREE OF

MASTER OF SCIENCE
IN
GEOLOGY AND GEOPHYSICS

MAY 2019
BY
MACEY SANDFORD

COMMITTEE:
PAUL LUCEY (CHAIR)
SHIV SHARMA
ROBERT WRIGHT

Abstract

New methods for optimizing data storage and transmission are required as orbital imaging spectrometers collect and downlink larger data volumes due to increases in optical efficiency and resolution. For missions investigating Earth surface reflectance, excising cloud-contaminated data during acquisition can significantly improve the overall science yield for a mission with a fixed downlink budget. Algorithms that consider threshold-based screening are able to operate at the data acquisition rate but require accurate and comprehensive prediction of cloud and surface brightness. Previous studies have not conducted a comprehensive analysis of a global dataset to provide appropriate thresholds for screening or to predict performance. To address this concern, the basis of our analysis used the Hyperion imaging spectrometer's historical archive of global Earth reflectance data. We selected a diverse subset that spans space (in latitudinal zone including the tropics, subtropics, arctic, and Antarctic), time (2005-2017), and wavelength (400 – 2500 nm) to assure that the distributions of cloud data were representative of all cases. We fit models of cloud reflectance properties gathered from the subset for the prediction of globally applicable thresholds. Distributions relate cloud reflectance properties to various surface types (land, water, and snow) and latitudinal zones. Models based on this dataset will be used to screen clouds onboard orbital imaging spectrometers, approximately doubling valuable science return per downlink.

Table of Contents

1 Introduction

Imaging spectrometers, also known as hyperspectral imagers, collect images in three dimensional data cubes: a two-dimensional image in the field of view and swath of the instrument with a continuous spectrum (depending on the instrument's spectral channels) in the third dimension. With the recent decommissioning of Hyperion, an imaging spectrometer onboard NASA's Earth Observer 1 (EO-1), many space agencies are considering or planning new orbital imaging spectrometer missions such as HISUI (Guanter et al., 2015), EMIT(Green et al., 2018), and EnMAP (Iwasaki et al., 2011). NASA is currently considering dramatically-enhanced imaging spectrometer architectures to provide measurements with global coverage (NASEM 2018). For all of these cases, it is expected that the instrument duty cycle will be limited by data volume. These instruments are operated with a store-and-forward mode (Williams et al., 2002), where the data is stored onboard in a limited "flight recorder" and can only be transmitted when a ground station is within view (or in the case of HISUI, when a manual transfer occurs). This limits the bandwidth from the satellite to the ground and thus the total data yield of the mission. Optimizing the downlink from orbital remote sensing satellites will increase the science yield of these missions. One way to avoid storing and downloading irrelevant data is to screen data images for spectral signatures onboard, as soon as they are collected (Thompson et al., 2014).

Previous studies indicate that clouds account for over half of the annual sky cover globally (Mercury et al., 2012, Eastman et al., 2011, King et al., 2013). However, neither the coverage nor the spectral appearance of clouds is uniform. Clouds cover more (68%) of the oceans on Earth annually than land (54%), and tropical regions have been noted to be exceptionally cloudy (Mercury et al., 2012, Eastman et al., 2011, King et al., 2013). Moreover, there is considerable zonal variability in cloud optical properties due to the different processes involved in their formation and evolution (Thompson et al., 2018). Finally, the optimal thresholds for a particular excision scenario also depend on the expected brightness of the land in that area of the globe (Thompson et al., 2014). Considering cloud fractions as a function of surface type and latitude could lead to more precise cloud detection.

To test this hypothesis, this study refines the cloud-screening algorithm previously introduced in Thompson et al. (2014). The original algorithm used three bands of interest to distinguish clouds from other surface types (El-Araby et al., 2005, Ackerman et al., 1998, Williams et al., 2002, Griffin et al., 2003). Here, we analyze the Hyperion global archive to provide globally-applicable models parameterized by latitude and surface type, enabling reflectance thresholds to predict the classification of cloud-contaminated data and non-cloud-contaminated data (land, water and snow). This study provides representative models for use by future orbital missions. We find that excising cloud-contaminated scenes will reduce onboard storage while at least doubling valuable science yield, per downlink.

2 Methods

Earth-orbiting imaging spectrometers that focus on surface reflectance properties typically ignore data contaminated with clouds. Screening spectroscopic data cubes for cloud-contaminated pixels onboard will allow for the downlink of more valuable science data. When screening a spectroscopic data cube for clouds, it is necessary to define the difference between data contaminated with clouds and data clear of clouds. Our data consist of pixels that are single locations within a scene, or image, which contain all the wavelengths measured by the spectrometer. The Hyperion hyperspectral imaging spectrometer, onboard NASA’s EO-1 satellite, collected a globally representative data set (Thompson et al., 2018) that we used for the classification of cloud-contaminated pixels. The Hyperion instrument’s measurement spans the 400 nm to 2500 nm interval of the electromagnetic spectrum. Top of Atmosphere (TOA) reflectance values, whose calculation accounts for observing geometry, were used to classify each pixel into four categories: land, water, snow and clouds. We curated and manually classified a sample set of 102 randomly selected images, producing distributions describing the frequency of observing each classification type based on their respective TOA values in each of the following wavelengths of interest: 447.17 nm, 1245.36 nm, and 1648.90 nm (Thompson et al., 2014). Our procedure is defined by the following steps: choose channels or bands that will be used to classify pixels, collect pixel brightness distributions of an historical dataset with respect to the factors of interest (surface type and latitude), and optimize channel thresholds given the distributions and false alarm requirements. With this information, we can predict optimal TOA values for screening clouds in *new* scenes based on advance knowledge of surface types and viewing geometry.

2.1 The Data Set

The Hyperion data set that spans wavelengths from 400 nm to 2500 nm was collected between 2005 and 2017. We selected three wavelengths of interest, namely 447.17 nm, 1245.36 nm, and 1648.90 nm, based on previous studies distinguishing clouds from land, water, and snow (Ackerman et al., 1998, Griffin et al., 2003, El-Araby et al., 2005, Thompson et al., 2014). Clouds and snow have a high reflectance in the 447 nm band while land and water do not. The near-infrared (1245 nm) and shortwave-infrared (1650nm) bands depict a difference in reflectance between clouds and snow. Snow has a slightly lower reflectance in the 1245 nm band than clouds while the 1650 nm band shows snow as even less reflective than clouds (Griffin et al., 2003). A subset of 102 Hyperion images were selected for our study over the full time range of the mission. This random set incorporated various sections of latitude to assure a global representation of measurements. The following latitudinal zones were included: Tropics (23.5°S to 23.5°N), Arctic (66.5°N to 90°N), Antarctic (66.5°S to 90°S), and Subtropics (66.5°S to 23.5°S and 23.5°N to 66.5°N). In this report, we refer to the Arctic and Antarctic latitudinal zones together as the Polar Regions. Due to the nature of the Hyperion data set where most measurements were taken over land, a sub set of longitudes ranging the Pacific Ocean (121°E to 180°E and 121°W to 180°W) were included to capture the spectral properties of water.

2.1 Classification

Accurate ground truth classifications are needed for the success of any statistically motivated algorithm. Pixels were hand-labeled to assure accuracy in classifying each surface type (Fig. 1). We use these data to relate pixels' TOA reflectance values to a classification of land, water, cloud or snow. After fitting this model, the manual classification of clouds can evaluate model classification accuracy. We only label opaque clouds; all pixels bordering various classification types were labeled as “ambiguous” to avoid any misclassification.

After manual labeling, we associate the surface types with the TOA reflectance value in each of the three bands of interest. This association produces three-dimensional frequency distributions of TOA reflectance values based on wavelength and surface type (Fig. 2). They describe the conditional probability of a pixel's TOA reflectance value given if it is a cloud or clear sky, c_1 and c_2 respectively ($P(y|c_{1,2})$). The non-cloud distribution, containing non-cloud surface types (land, water, and snow), is also separable into each surface type. To understand how clouds are classified from various surface types and as a function of latitude, we represent the distributions as a function of these parameters, $P(y|x,c)$, where x is the surface type or zone of interest.

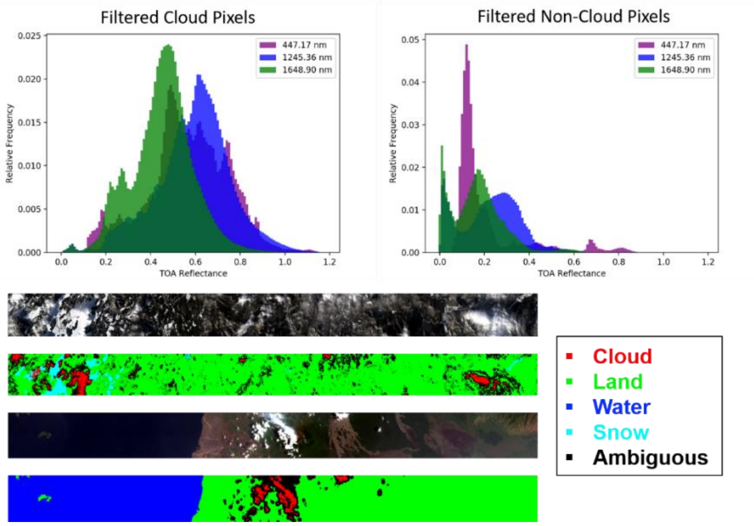

Figure 1. An example of the one-dimensional distributions of clouds and non-clouds in each wavelength (top) created from the hand-labeled pixels in the Hyperion images (bottom).

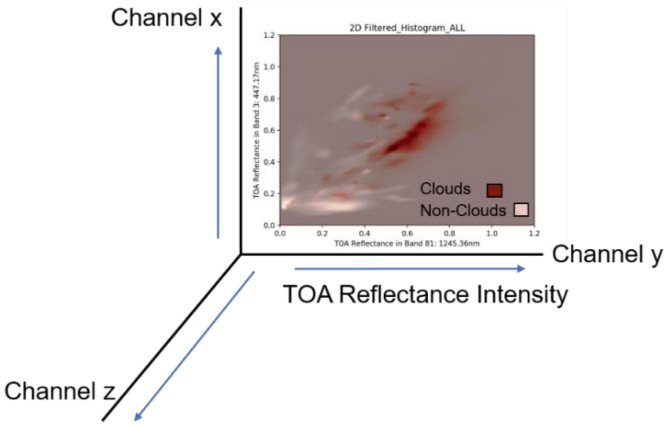

Figure 2. Cloud and non-cloud brightness distributions, with an example marginal distribution in one plane.

2.2 Algorithm

Our cloud-screening approach predicts scene-specific thresholds in three bands of interest for real-time use onboard (Thompson et al., 2014). In general, a cloud-screening algorithm must define an **exclusion region** $R \subseteq \mathbb{R}^d$, i.e a range of TOA reflectance values for which the pixel is considered to be cloudy. The cloud-screening approach maps the pixel brightness values to a binary classification c=f(**y**): $\mathbb{R}^d \mapsto \{c_1, c_2\}$. A vector **y** is representative of a spectrum from a given pixel. Thus, the decision rule for this classification is,

$$f(\boldsymbol{y}) = \begin{cases} c_{1,}\ if\ \boldsymbol{y} \in \mathrm{R} \\ c_{2,}\ if\ \boldsymbol{y} \notin \mathrm{R} \end{cases}$$

where R is defined with a set of thresholds, φ (in this case a triplet). Any pixel exceeding all three thresholds simultaneously is classified as cloud-contaminated (Fig. 3).

The following expected loss function considers α_{FP} and α_{FN} as the false positive and negative penalties, respectively,

$$E[\mathcal{L}] = \int_R \alpha_{FP} P(c_1|\boldsymbol{y},\boldsymbol{x})d\boldsymbol{y} + \int_{\mathbb{R}^d/R} \alpha_{FN} P(c_2|\boldsymbol{y},\boldsymbol{x})d\boldsymbol{y}$$

A false positive penalty considers the cases where clear pixels are classified as cloud contaminated. P(y|c_1) and P(y|c_2) are the probability of encountering a cloud-contaminated pixel and a clear pixel, respectively. P(c_1) and P(c_2) are the prior probability of clouds and clear sky based on an historical average, respectively. Minimizing this function yields the optimal threshold for any given factors, defined by **x.** Using Bayes' rule and assuming independence (Thompson et al. 2014), the expected loss function can be decomposed into the respective likelihoods and priors for the posterior described above,

$$E[\mathcal{L}] = \int_R \alpha_{FP} P(\boldsymbol{y}|\boldsymbol{x}, \boldsymbol{c_1}) P(c_1) d\boldsymbol{y} + \int_{\mathbb{R}^d/R} \alpha_{FN} P(\boldsymbol{y}|\boldsymbol{x}, \boldsymbol{c_2}) P(c_2) d\boldsymbol{y}$$

Thus, we can use the likelihood, or sampling distribution, created from the Hyperion sample set to minimize our expected loss and produce predictive thresholds for screening.

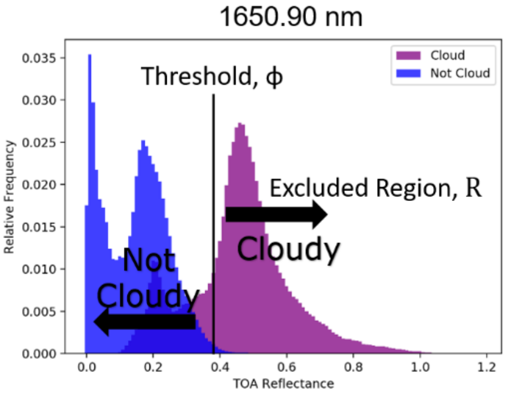

Figure 3. Depiction of the exclusion region, in the 1650.90 nm band, for which to classify cloud-contaminated data. A pixel with a TOA reflectance exceeding the threshold, φ, is classified as cloudy and anything below the threshold is classified as non-cloudy. Note that this is one-dimensional, and to be classified as cloudy in our algorithm, the TOA reflectance must exceed the threshold in each band simultaneously.

3 Results

The model used for cloud-screening was developed using cloud brightness distributions in TOA values as a function of time, space, and wavelength. The brightness distributions collected from the

Hyperion sample set represent cloud and non-cloud brightness values in TOA units, for each band (447.17 nm, 1245.36 nm, 1648.90 nm). The breadth of the scenes in the dataset span the globe (Table 1).

Table 1. The number of images in the Hyperion sample set (102 images) collected in each global region. The ocean category includes images taken in the regions of Tropics, Subtropics, and Polar Regions.

Hyperion Image Dataset Breakdown

Global Region	Number of Images
Tropics	30
Subtropics	51
Polar Regions	21
ALL	**102**
Ocean Sub Set	19

The output of the algorithm is a threshold triplet that defines the region of TOA reflectance values that classify cloud-contaminated data, i.e. the exclusion region (discussed in section 2.3). The penalties in the expected loss function determine our tolerance for errors; a higher false positive penalty yields a more conservative threshold and a smaller exclusion region. Minimizing this penalty requires that the exclusion region consider the expected surface properties. For example, since clouds and snow have similar reflective properties in two of the bands used, one could use a more conservative threshold triplet to screen clouds in Polar Regions. The repercussions of a conservative threshold (α_{FP}=1000) calculation, a moderate threshold (α_{FP}=100) calculation, and a less conservative threshold (α_{FP}=10) calculation are shown in a two-dimensional histogram representing all scenes in the dataset (Fig. 4).

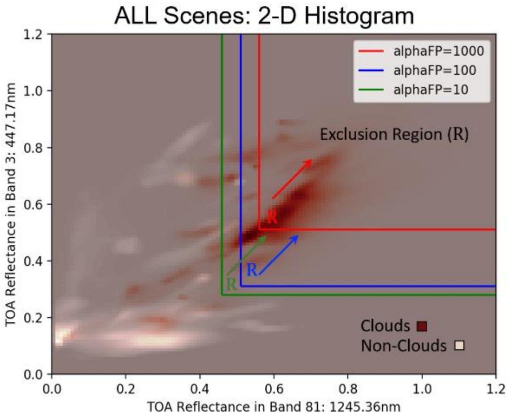

Figure 4. A Two-dimensional histogram of cloud and non-cloud distributions for the Hyperion dataset. The exclusion region for various false positives are shown as colored rectangles; α_{FP}=1000 (red), α_{FP}=100 (blue), α_{FP}=10 (green). The color gradient of the data indicates relative frequency.

The optimal (i.e. minimizing the loss) thresholds at various false positive rates using the Hyperion sample set are shown in Table 2. The thresholds are defined differently for each latitudinal zone. The Discussion section (Section 4) describes statistical validation tests used to ensure the size and breadth of our subset, or sampling distribution, to predict these thresholds for future scenes.

Table 2. Optimal Thresholds in TOA (Top of Atmosphere) reflectance values using a false negative of 1 for each latitudinal zone.

Optimal Thresholds for Screening Clouds

False Positive Value	Latitudinal Zone	447.17 nm	1245.90 nm	1649.36 nm
1000	Tropics	0.31	0.34	0.13
	Subtropics	0.52	0.36	0.24
	Polar Regions	0.47	0.57	0.30
	Ocean	0.41	0.37	0.30
	ALL	**0.51**	**0.56**	**0.29**
100	Tropics	0.27	0.25	0.13
	Subtropics	0.31	0.51	0.23
	Polar Regions	0.55	0.27	0.22
	Ocean	0.39	0.34	0.28
	ALL	**0.31**	**0.51**	**0.22**
10	Tropics	0.26	0.21	0.11
	Subtropics	0.28	0.45	0.22
	Polar Regions	0.54	0.26	0.20
	Ocean	0.32	0.25	0.22
	ALL	**0.28**	**0.46**	**0.22**

4 Discussion

The study of a globally representative sample set of imaging spectroscopy data provided a deeper understanding of TOA reflectance for various surface types in space, time, and wavelength and a prediction model for screening cloud-contaminated data onboard orbital imaging spectrometers. This section discusses our findings concerning cloud brightness, including a literature comparison concerning cloud fractions in our dataset, the empirical error of our dataset, and the potential improvement yield of downlink using this cloud-screening algorithm.

4.1 Cloud Brightness

The Hyperion global dataset was sampled and manually classified to understand cloud brightness as a function of time, space, and wavelength. We collected the TOA values in a 3-dimensional histogram, one axis for each wavelength studied. This yields a probability distribution of TOA values of clouds globally that we can use to predict the classification of TOA values for future scenes. In order to verify if classifying clouds depending on their global region would produce a lower false alarm rate, we subset our scenes into latitudinal zone and surface type.

Table 3. Mean values of the distributions of TOA reflectance for each classification type, at each selected wavelength. The change in values across this table verifies the advantage of presenting screening thresholds as a function of latitudinal zone.

Cloud Brightness *mean* values

Longitudinal Zone	447.17 nm	1245.36 nm	1650.90 nm
Tropics	0.47	0.61	0.50
Subtropics	0.57	0.61	0.45
Polar Regions	0.75	0.47	0.45
Ocean	0.49	0.49	0.44
ALL	**0.49**	**0.61**	**0.48**

Our results show that mean cloud TOA brightness differs in the bands studied in the Tropics, Arctic, Antarctic, Subtropics, and Pacific Ocean zones. The mean TOA reflectance values for each global region, in each wavelength is presented in Table 3. The difference in these mean values indicates that the optimal thresholds assigned for the classification of clouds in each area should also differ (Table 2). Further statistical analysis is necessary to properly quantify and interpret these differences and will be carried out before submitting for publication.

The distributions show that TOA reflectance differs with surface type concerning the wavelength bands used. Cloudy pixels have higher TOA reflectance values in the wavelengths given while non-cloudy pixels have generally lower TOA values. Specifically, pixels with snow have low TOA reflectance values at 1250 nm and even lower TOA reflectance values at 1650 nm, while having strong TOA reflectance properties at 447 nm. Generally, our data aligns with the general properties of non-cloud surface types discussed in Ackerman et al., 1998. Again, further statistical analysis is necessary to properly quantify and interpret these differences and will be carried out before submitting for publication.

4.2 Empirical Error Tests

Quantifying cloud excision performance is essential. Based on parameters such as latitudinal zone and surface type, we can determine the achievable performance window of the algorithm; where the most clouds are excised with the least amount of mistaken classification. Screening classification depends largely on the false positive parameter (Fig. 5).

We performed a leave-one-out cross-validation experiment, recalculating thresholds 102 times and excluded a different validation scene from each trial. Every test conducted (102) resulted in the same thresholds presented in Table 3. This is one validation that a single scene does *not* define the optimal margin for the distribution for the brightness resolution of our lookup table. This confirms that our dataset is sufficient in space, time and wavelength to predict optimal thresholds for future scenes.

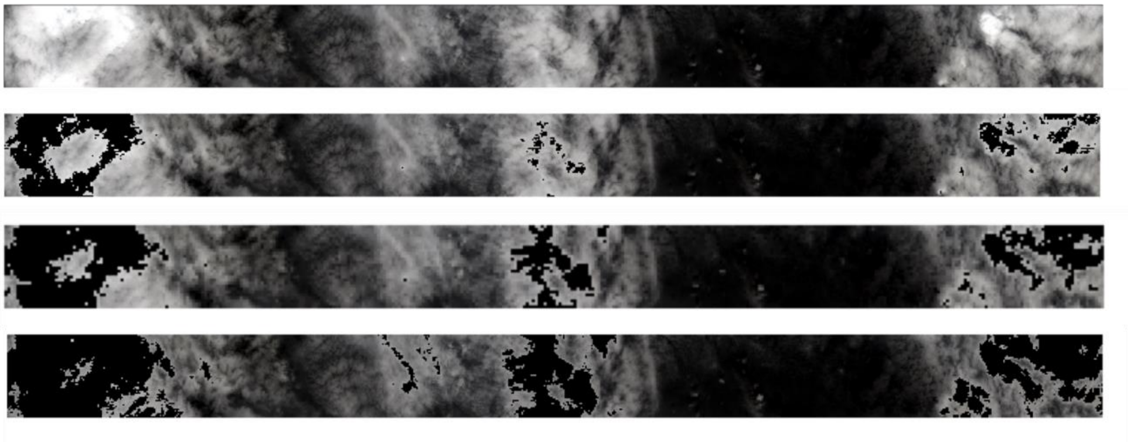

Figure 5. An example of pixels classified as cloudy being excised from the image. The top image is the raw image with no screening, the second image is cloud-screening with α_{FP}=1000, the third image is cloud-screening with α_{FP}=100, and the fourth image is cloud-screening with α_{FP}=10.

4.3 Potential Improvement yield of screening

A case study of the EMIT (Earth Surface Mineral Dust Source Investigation) mission quantified the improvement achievable, specifically for similar Earth orbiting imaging spectrometers (Table 4). The EMIT mission will be launched to the International Space Station, with an orbit dominated by low-latitude regions (Green et al., 2018). We simulated cloud cover fractions using pre-calculated global cloud probabilities (x) from historical MODIS data (Mercury et al., 2012), defined as an annual average cloud cover probability at a spatial resolution of one degree. We simulated ISS observations at a 10 second rate for one year, starting on February 1st, 2022. The high improvement yields indicate the significance of screening cloud-contaminated data for missions concerned solely with ground reflectance data. Using the cloud-screening tool presented, we predict at least double the current return of useful data in all specific regions, and overall. It is important to note the difference in improvement yield when considering all regions at once and when considering one region at a time. The difference in improvement yield shows that some areas of the globe are cloudier than others, so the benefit of using a cloud-screening tool is particular to the region(s) of interest.

Table 4. A case study of EMIT (Earth Surface Mineral Dust Source Investigation) concerning a global cloud fraction simulation was used to determine the improvement yield of the cloud-screening tool in terms of latitudinal region.

Improvement Yield based on Case Studies

Case Study	Simulated Cloud Coverage Observed (%)	Improvement Yield (Factor of increase in usable data)
EMIT	Tropics: 65%	x2.38
	Subtropics: 57%	x2.85
	Arctic: 52%	x2.32
	Antarctic: 50%	x2.08
	All Regions: 58%	**x2.04**

As previously discussed, past literature presents cloud cover fractions that are greater over land than water and that tropical regions are more cloudy than other global regions (Eastman et al., 2012, Ackerman et al., 1998). The EMIT case study cloud fractions show that cloud cover in the tropics is greater than any other region studied. We cannot present cloud fractions for the Ocean region since the simulated data only occurred at coordinates over land. Before submitting for publication, we will also conclude a case study for another future mission by ESA (European Space Agency).

5 Conclusion

The newly improved method described in Thompson et al. (2014) for screening cloud-contaminated data onboard orbital imaging spectrometers will at least double the downlink of more useful data. This was done by collecting and studying a globally representative data set and producing screening thresholds based on latitude and surface type. Using latitude and surface type as a parameter in screening clouds will help correctly classify could-contaminated pixels while reducing misclassifications of other surface types. The overall yield of useful data doubles when using this screening algorithm. Thus, the newly improved cloud screening tool is an important improvement in reducing storage and downlink onboard orbital imaging spectrometers.

In all, this method introduces the optimization of onboard data storage and downlink from orbital imaging spectrometers using a cloud-screening tool (Table 4) with optimized thresholds (Table 2). We also developed a subsequent representation of cloud brightness (TOA reflectance values) in the 447.17 nm, 1249.36 nm, and 1650.90 nm wavelengths that change with latitude and surface type (Table 3).

Acknowledgements

I would like to thank Dr. David Thompson at NASA JPL for the opportunity to work on this project and for guidance along the way, the JPL Summer Internship Program for allowing me the ability to be a part of such an opportunity, Dr. Robert Green and the Imaging Spectroscopy group for funding and providing office space to work, and my advisors Shiv Sharma and Anupam Misra at UH for lending me the time to work at NASA JPL to complete this project.

References

Ackerman, S. A., K. I. Strabala, W. P. Menzel, R. A. Frey, C. C. Moeller, and L. E. Gumley, "Discriminating clear sky from clouds with MODIS," *J. Geophys. Res., Atmosp.*, vol. 103, no. D24, pp. 32 141–32 157, Dec. 1998.

Eastman, R., S. Warren, and C. Hahn, "Variations in cloud cover and cloud types over the ocean from surface observations, 1954–2008," in *J. Climate*, Nov. 2011, vol. 24, no. 22, pp. 5914–5934.

El-Araby, E., M. Taher, T. El-Ghazawi, and J. Le Moigne, "Prototyping automatic cloud cover assessment (ACCA) algorithm for remote sensing on-board processing on a reconfigurable computer," in *Proc. IEEE Int. Conf. Field-Programm. Technol.*, 2005, pp. 207–214.

Green, R. O., N. M. Mahowald, R. N. Clark, B. L. Ehlmann, P. A. Ginoux, O. V. Kalashnikova, R. L. Miller, G. Okin, T. H. Painter, C. Pérez García-Pando, V. J. Realmuto, G. A. Swayze, D. R. Thompson, E. Middleton, L. Guanter, E. Ben Dor, B. R. Phillips, "NASA's Earth Surface Mineral Dust Source Investigation," American Geophysical Union, Fall Meeting 2018, abstract #A24D-01.

Griffin, M. K., H. K. Burke, D. Mandl, and J. Miller, "Cloud cover detection algorithm for EO-1 hyperion imagery," in *Proc. 17th SPIE AeroSense Conf. Algorithms Technol. Multispectral, Hyperspectral Ultraspectral Imagery IX*, Orlando, FL, USA, 2003.

Guanter, L., H. Kaufmann, K. Segl, S. Foerster, C. Rogass, S. Chabrillat, T. Kuester, A. Hollstein, G. Rossner, C. Chlebek, C. Straif, S. Fischer, S. Schrader, T. Storch, U. Heiden, A. Mueller, M. Bachmann, H. Mühle, R. Müller, M. Habermeyer, A. Ohndorf, J. Hill, H. Buddenbaum, P. Hostert, S. van der Linden, P. Leitão, A. Rabe, R. Doerffer, H. Krasemann, H. Xi, W. Mauser, T. Hank, M. Locherer, M. Rast, K. Staenz, B. Sang (2015), "The EnMAP Spaceborne Imaging Spectroscopy Mission for Earth Observation," Remote Sens. 2015, 7(7), 8830-8857; doi: 10.3390/rs70708830.

Iwasaki, A., N. Ohgi, J. Tanii, T. Kawashima, H. Inada (2011). Hyperspectral Imager Suite (HISUI)-Japanese hyper-multi spectral radiometer, “International Geoscience and Remote Sensing Symposium (IGARSS),” 1025-1028. 10.1109/IGARSS.2011.6049308.

King, M., S. Platnick, W. Menzel, S. Ackerman, and P. Hubanks, “Spatial and temporal distribution of clouds observed by MODIS onboard the Terra and Aqua satellites,” *IEEE Trans. Geosci. Remote Sens.*, vol. 51, no. 7, pp. 3826–3852, Jul. 2013.

Mercury, M., R. Green, S. Hook, B. Oaida, W. Wu, A. Gunderson, and M. Chodas, “Global cloud cover for assessment of optical satellite observation opportunities: A HyspIRI case study,” *Remote Sens. Environ.*, vol. 126, pp. 62–71, Nov. 2012.

National Academies of Sciences, Engineering, and Medicine. 2018. “Thriving on Our Changing Planet: A Decadal Strategy for Earth Observation from Space,” Washington, DC: The National Academies Press. https://doi.org/10.17226/24938.

Salomonson, V. V. and I. Appel, “Estimating fractional snow cover from MODIS using the normalized difference snow index,” in *Remote Sens. Environ.*, Feb. 2004, vol. 89, no. 3, pp. 351–360.

Thompson, D. R., et al. “Global Spectroscopic Survey of Cloud Thermodynamic Phase at High Spatial Resolution, 2005–2015.” Atmospheric Measurement Techniques, vol. 11, no. 2, 2018, pp. 1019–1030., doi:10.5194/amt-11-1019-2018.

Thompson, D. R., et al. “Rapid Spectral Cloud Screening Onboard Aircraft and Spacecraft.” Geoscience and Remote Sensing, IEEE Transactions On, vol. 52, no. 11, 2014, pp. 6779–6792., doi:10.1109/TGRS.2014.2302587.

Williams, J. A., A. S. Dawood, and S. J. Visser, “FPGA-based cloud detection for real time onboard remote sensing,” in *Proc. IEEE Int. Conf. Field-Programm. Technol.*, 2002, pp. 110–116.